Dislocation creep of olivine: Low-temperature plasticity controls transient creep at high temperatures

Lars N. Hansen[1]*, David Wallis[2†], Thomas Breithaupt[3], Christopher A. Thom[3], Imogen Kempton[3]

[1]Department of Earth and Environmental Sciences, University of Minnesota, Minneapolis, 55455, United States of America

[2]Department of Earth Sciences, Utrecht University, Utrecht, 3584 CB, The Netherlands

[3]Department of Earth Sciences, University of Oxford, Oxford, OX1 3AN, United Kingdom

[†]Present address: Department of Earth Sciences, University of Cambridge, Cambridge, CB2 3EQ, United Kingdom

*corresponding author: lnhansen@umn.edu

Keywords: olivine, dislocation creep, transient creep, backstress, dislocation interactions, stress-reduction tests, mantle viscosity

Abstract

Transient creep occurs during geodynamic processes that impose stress changes on rocks at high temperatures. The transient is manifested as evolution in the viscosity of the rocks until steady-state flow is achieved. Although several phenomenological models of transient creep in rocks have been proposed,

the dominant microphysical processes that control such behavior remain poorly constrained. To identify the intragranular processes that contribute to transient creep of olivine, we performed stress-reduction tests on single crystals of olivine at temperatures of 1250–1300°C. In these experiments, samples undergo time-dependent reverse strain after the stress reduction. The magnitude of reverse strain is ~10^{-3} and increases with increasing magnitude of the stress reduction. High-angular resolution electron backscatter diffraction analyses of deformed material reveal lattice curvature and heterogeneous stresses associated with the dominant slip system. The mechanical and microstructural data are consistent with transient creep of the single crystals arising from accumulation and release of backstresses among dislocations. These results allow the dislocation-glide component of creep at high temperatures to be isolated, and we use these data to recalibrate the low-temperature plasticity flow law for olivine to describe the glide component of creep over a wide temperature range. We argue that this flow law can be used to estimate both transient creep and steady-state viscosities of olivine, with the transient evolution controlled by the evolution of the backstress. This model is able to predict variability in the style of transient (normal versus inverse) and the load-relaxation response observed in previous work.

1 Introduction

The evolution of viscosity during flow of mantle rocks at high temperatures is fundamental to a variety of geodynamic processes. For example, transient creep of the upper mantle has been identified as a major contributor to geodetically observed surface deformations during post-seismic creep (Freed et al., 2012; Masuti et al., 2016; Pollitz, 2005; Qiu et al., 2018), for which the strains are typically <10^{-3}, and inferred viscosities are one to two orders of magnitude lower than the long-term, steady-state viscosity. Because transient viscosities also continue to evolve during postseismic deformation, they likely cause a time-dependent transfer of stresses to neighbouring faults, rather than the instantaneous transfer assumed by popular calculations of Coloumb stress changes (e.g., Freed, 2005). Although sophisticated earthquake

forecast models do incorporate time-dependent loading according to average plate motion rates (Field et al., 2017, e.g., 2015), they still do not incorporate variable loading rates that would occur due to transient creep of the lithosphere. In addition, transient viscosities are expected to be important, although have not yet been thoroughly considered, in other small-strain processes including flexure of the lithosphere near volcanic loads (Zhong and Watts, 2013) or in subducting slabs near trenches (Hunter and Watts, 2016), during which the strains rarely exceed 10^{-2}.

Although by far the bulk of investigations into the rheological behavior of the upper mantle have focused on measuring and predicting steady-state viscosities in olivine attained under constant applied stress (e.g., Hirth and Kohlstedt, 2003), some experiments have been conducted to investigate transient creep in olivine. These experimental data confirm that the initial viscosities at the onset of creep or just after other abrupt changes in stress are typically several orders of magnitude lower than the eventual steady-state viscosities (Chopra, 1997; Hanson and Spetzler, 1994; Post, 1977; Smith and Carpenter, 1987). These rapid changes in viscosity that occur over the initial strain increments of $<10^{-2}$ are associated with subtle changes in microstructure that are intimately tied to the steady-state viscosities reached at higher strains. The most likely microstructural changes responsible for this evolution are changes in dislocation density and rates of dislocation glide (Durham et al., 1977; Hanson and Spetzler, 1994; Karato and Spetzler, 1990). However, there are certain cases in which the initial viscosity is higher at the onset of creep and decreases with progressive deformation, which is referred to as an “inverse” transient. Hanson and Spetzler (1994) observed that single crystals of olivine can exhibit either a normal or an inverse transient, depending on the orientation of loading. In addition, Cooper et al. (2016) observed that the type of transient can change in a single experiment as the applied stress is gradually increased. This variability in observations highlights that the specifics of the microstructural evolution and its link to both transient creep and steady-state creep remain poorly constrained.

Due to the complexity of, and uncertainty regarding, potential micromechanical processes involved, experimental observations of transient creep have generally been fit by empirical models in which the underlying physics is not investigated. The Burgers model is often employed (Chopra, 1997; Smith and Carpenter, 1987), amongst several others (Hanson and Spetzler, 1994; Post, 1977). However, the lack of a rigorous microphysical basis to these models limits confidence in extrapolating them to predict deformation at natural conditions under which the key processes potentially differ from those in experiments. Moreover, as these processes and associated microstructural changes are poorly constrained, model predictions cannot be tested against the microstructures of natural rocks. Thus, there is a need to establish the fundamental microphysics of transient creep.

Distinguishing among different models of transient creep is difficult. In general, the experimentalist is tasked with fitting models to strain-time curves or strain rate-time curves, for which differences among models are subtle (Hanson and Spetzler, 1994; Post, 1977). Additional constraints can potentially be gleaned from the microstructures of deformed materials (Hanson and Spetzler, 1994). However, the small strains involved can result in microstructural changes beyond the resolution of some common observational techniques, such as standard electron backscatter diffraction (EBSD) (Thieme et al., 2018).

We alleviate these problems by using stress-reduction experiments. These tests involve applying a rapid reduction in stress to a sample undergoing steady-state creep and have been applied extensively to the study of engineering materials (Biberger and Gibeling, 1995; Blum and Weckert, 1987; Poirier, 1977). Stress reductions typically induce an ensuing period of transient creep. As each test requires only a small strain interval and causes only limited modification of the microstructure, multiple tests can be performed on a sample within one experiment (e.g., with different magnitudes of stress reduction). Unlike increases in stress magnitude, which are always followed by ongoing creep in the original direction, reductions in stress can also result in a period of anelastic reverse strain (Biberger and Gibeling, 1995; Blum and

Weckert, 1987; Poirier, 1977). As such, stress-reduction tests provide a wide variety of characteristics against which to test models of transient creep.

Despite their potential, stress-reduction tests have been underutilized for geological minerals. Stress-reduction tests have been applied to ice (Caswell et al., 2015; Meyssonnier and Goubert, 1994) and garnet (Wang et al., 1996). Applications to olivine have been limited primarily to torsional microcreep experiments on fine-grained aggregates by Gribb and Cooper (1998) and Jackson et al. (2014, 2002). Chopra (1997) reported two experiments on natural dunites, and Cooper et al. (2016) reported one experiment on a single crystal. However, the microphysical controls on the behaviour exhibited in such tests have not been systematically investigated.

Here we report stress-reduction experiments on single crystals of olivine to isolate and investigate transient creep arising from intragranular processes. We analyse the microstructures of the deformed samples using high-angular resolution electron backscatter diffraction (HR-EBSD) (Wallis et al., 2019; Wilkinson et al., 2006), which is ideally suited to detecting subtle microstructural changes, including lattice rotations and stress heterogeneities associated with geometrically necessary dislocations (GNDs). We combine the results with previous rheological data to constrain the microphysical processes that control the transient viscosity of rocks after rapid stress changes and make predictions about the variability in rheological behavior that may be observed during transient creep in Earth.

2 Methods

2.1 Sample preparation

Four samples were prepared from gem-quality single crystals of San Carlos olivine. Rough crystals were oriented using EBSD. The crystals were cut into rectangular parallelepipeds, with lengths in the range of

2 to 5 mm and aspect ratios in the range of 2:1 to 3:1, that were free from visible cracks and inclusions. Samples were cut with long axes corresponding to the $[110]_c$, $[101]_c$, and $[011]_c$ orientations, following the notation of Durham and Goetze (1977), with the intention of maximizing the resolved shear stress on the (010)[100], (001)[100] and (100)[001], and (010)[001] slip systems, respectively. The end faces of samples were ground flat and parallel using 1500 grit SiC paper.

2.2 Deformation experiments

Deformation experiments were conducted in a 1-atm uniaxial creep apparatus in the Rock Rheology Laboratory at the University of Oxford. Details of the apparatus design are provided by Cao et al. (2020). Samples were placed in direct contact with alumina platens, which were in direct contact with SiC pistons. Although San Carlos olivine and alumina are not in chemical equilibrium, reaction products were not visible after experiments, indicating that any reaction was limited in extent. The loading column is housed inside a vertical tube furnace. The hot zone of the furnace is >5 cm, and temperature was controlled with a thermocouple placed within 1 cm of the sample. The temperature difference across the samples was <1°C. The oxygen fugacity was controlled with a mixture of CO and CO_2, and the ratio of gas flow rates was maintained constant to set the oxygen fugacity at a value of 10^{-8} to $10^{-7.5}$ atm, near the Ni:NiO buffer at the temperatures of the experiments. A gas-tight seal was maintained on the moving SiC piston by means of frictionless oil bellows. An axial load was applied to the loading column with a piezoelectric actuator using a closed-loop servo-control system, and the load was measured and controlled with a precision of ~1 N. Changes in sample length were assessed by measuring displacements of the SiC piston relative to the loading frame. Displacements were measured with a linear encoder with resolution of 10 nm and corrected for distortion of the apparatus using the complex compliance of the apparatus calibrated by Cao et al. (2020).

Samples were initially subjected to a small compressive load (~10 N) using the piezoelectric actuator to ensure that contact was maintained with pistons and the sample remained upright and aligned throughout the heating procedure. Samples were heated to temperatures of either 1250 or 1300°C over the course of approximately 3 hours. Deformation was not initiated until the measured temperature reached and maintained a steady value within 1°C of the set point.

Once the temperature stabilized, the load was gradually increased at a constant rate to the desired value, corresponding to stresses of 77 to 189 MPa, over the course of ~120 s. An example of the stress and strain evolution for experiment OxR0009 is illustrated in Figure 1. The load was maintained at the desired value, and the displacement was monitored until an approximately steady-state displacement rate was achieved, which typically required 2 to 5% strain. At this point, the load was reduced to a new set point at the maximum rate achievable by the apparatus, which was on the order of ~10 ms for the largest stress reductions. In order to record this deformation with sufficient resolution, the data sampling rate was increased from 0.1 Hz to 100 kHz just prior to the load reduction and then returned to 0.1 Hz just after the load reduction. This new load was maintained and the displacement monitored until a positive displacement rate was clearly observed. The load was then gradually increased back to the original value at a similar loading rate as in the initial loading increment. The load was then held constant until a steady-state displacement rate was again achieved. This cycle of load reduction followed by a return to the original load was carried out multiple times in each experiment. In each cycle, the load was reduced a greater amount than in the previous cycle, but after each load reduction, the load was always returned to the original control value. For several experiments, this progression of load reductions was repeated to test the reproducibility of the sample response. An overview of the experimental conditions are provided in Table 1.

Table 1: Summary of experiment conditions and results from stress-reduction experiments.

Sample #	Loading	Temperature	Initial stress	Steady-state	Best-fit	Best-fit	Transient	Symbol in

Experiment #	direction	(°C)	(MPa)	strain rate (10^{-5} s^{-1})	backstress (MPa)	hardening coefficient, γ		figures
OxR0002 170120c	$[101]_c$	1250	162	3.76	84	14	inverse	■
OxR0007 170323	$[110]_c$	1250	189	5.81	102	28	inverse	▶
OxR0009 170616	$[110]_c$	1300	105	1.95	64	12	unclear	◁
OxR0009 171018	$[110]_c$	1300	77	1.31	39	5	inverse	△
OxR0010 171016	$[011]_c$	1300	116	0.12	104	55	normal	○

Experiments were stopped after an increment of deformation at the original load value. This final load value was maintained until steady-state displacement rates were obtained so that the preserved microstructure best reflects the microstructure just prior to each load reduction. At this point, the load was removed entirely from the sample and the furnace was shut off. Cooling to ambient temperature required several hours, but temperatures fell below 800°C in ~3 min, which is rapid enough to preserve the microstructures characteristic of the highest stresses applied (Bai and Kohlstedt, 1992a; Goetze and Kohlstedt, 1973).

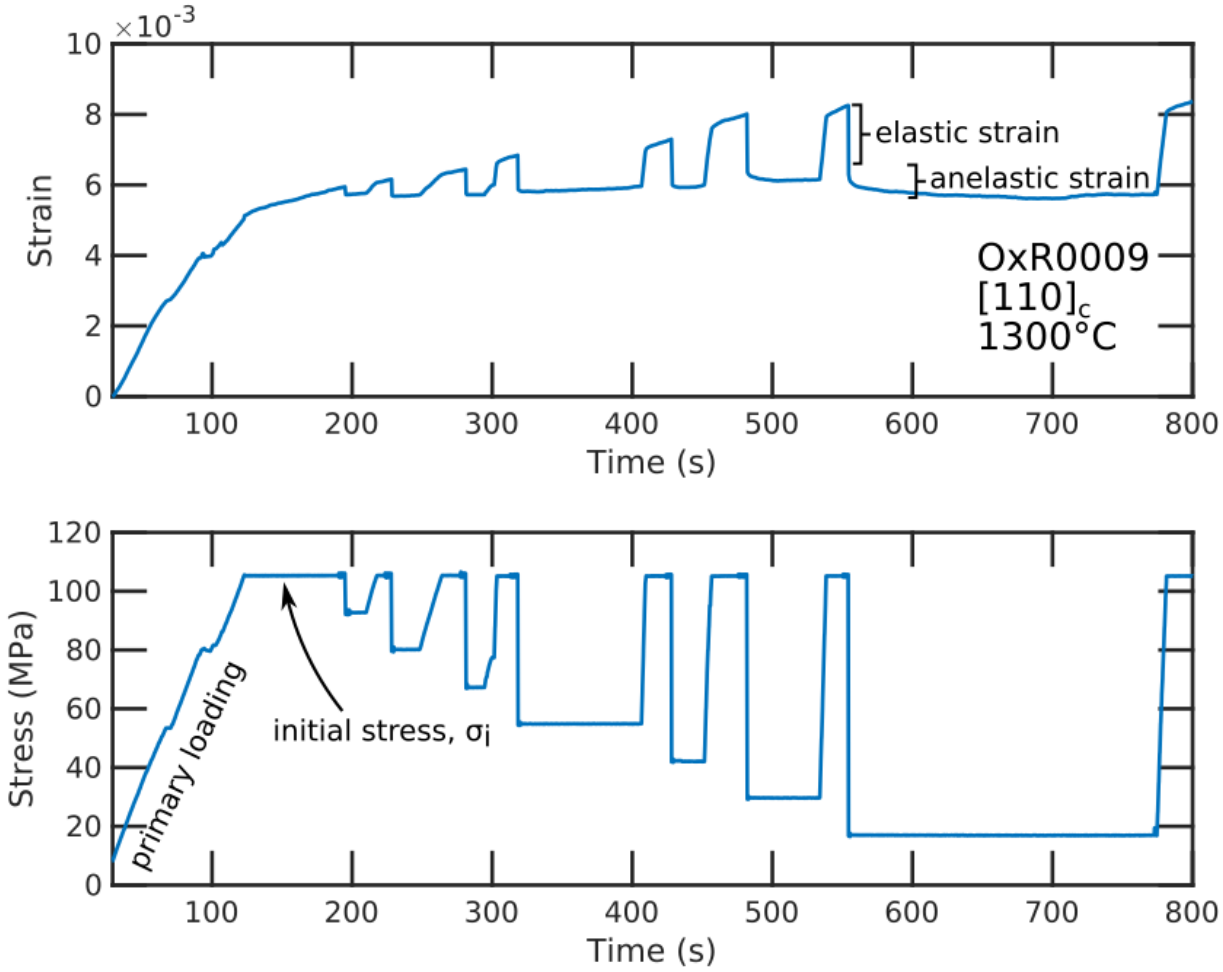

Figure 1: Axial strain and stress as functions of time for the first 800 s of deformation of sample OxR0009. Seven stress reductions are illustrated after the primary loading phase. The initial stress used to set the microstructure was 105 MPa. After each stress reduction, the reverse strain was composed of both an elastic and an anelastic component, as denoted by annotations. Elastic strains in this figure are a combination of the elastic distortion of both the apparatus and the sample.

2.3 Microstructural analysis

For one experiment (OxR0009, compressed along $[110]_c$), the microstructures within the sample were characterized after two segments of deformation. The experiment was initially interrupted at 7% strain. At this point, the face parallel to (001) was polished with successively finer diamond grits down to a grit size of 50 nm, providing a polish suitable for EBSD. An initial EBSD map was collected in an area of high

surface quality near the bottom of the polished vertical face of the sample. The sample was then reloaded into the apparatus and subjected to further increments of deformation. The experiment ended after a total of 38% strain. Two additional EBSD maps were collected on the same sample surface parallel to (001). One of these maps was located near the center of the sample and the other near a vertical edge.

The EBSD maps of sample OxR0009 were constructed using high-angular resolution electron backscatter diffraction (HR-EBSD). Data were acquired on an FEI Quanta 650 scanning electron microscope at the University of Oxford and a Philips XL30 scanning electron microscope at Utrecht University. Both instruments were equipped with an Oxford Instruments AZtec EBSD system and calibrated for HR-EBSD analysis by mapping undeformed Si standards following the procedure of Wilkinson et al. (2006). A routine to calibrate the chamber geometry, based on determining the pattern centre from diffraction patterns collected at a range of camera insertion distances, was performed before acquisition of each dataset. Conventions for reference frames in data acquisition and processing were validated using the approach of Britton et al. (2016). The details of each map are presented in Table 2.

Table 2: Details of HR-EBSD maps collected from sample OxR0009. The first map was collected after experiment 170616, and the subsequent maps were collected after experiment 171018. See Table 1 for details of the experiments.

Total strain	Map location on sample surface	Step size (μm)	Number of points	Pixels in diffraction pattern
7%	Bottom edge	3.0	230 x 150	1344 x 1024
38%	Centre	0.3	300 x 250	1344 x 1024
38%	Side edge	0.5	230 x 160	1344 x 1024

Maps of lattice rotation and elastic strain heterogeneity were generated following the HR-EBSD post-processing method of Wilkinson et al. (2006) and Britton and Wilkinson (2012, 2011). 100 regions of interest in each diffraction pattern were cross correlated with a reference pattern chosen within each

map. Shifts in the regions of interest were used to estimate the deformation gradient tensor, which was decomposed into rotations and strains, at each point the map. The pattern remapping approach of Britton and Wilkinson (2012) allows elastic strain measurements in the presence of lattice rotations of several degrees. Stresses were estimated from the elastic strain measurements following the approach of Britton and Wilkinson (2012) and employing the elastic constants for olivine at room temperature from Abramson et al. (1997). Measured elastic strains are relative to the unknown strain state of the reference point and therefore provide maps of stress heterogeneity. We rotated measured stress tensors from the reference frame of the EBSD maps into the reference frames of the measured crystal orientations to obtain the shear stresses resolved on each slip system (Wallis et al., 2017). A comprehensive overview of all data acquisition and processing procedures for HR-EBSD is provided by Wallis et al. (2019).

3 Results

3.1 General creep behavior

Figure 1 presents stress and strain as a function of time for the first 800 s of experiment 170616 with sample OxR0009, which is a typical example of the response of all samples. In this particular experiment, the strain rate did not significantly evolve, but was instead approximately constant over the first ~1% of strain. In other experiments, the strain rate after initial loading was observed to decrease or increase with progressive strain before a steady-state strain rate was reached, which we refer to as “normal” or “inverse” transients, respectively. Table 1 indicates the type of transient observed for each experiment. Figure 1 also illustrates that, once a steady-state strain rate was clearly achieved, stress reduction tests were executed. At the end of each reduction test, the stress was increased to approximately the same value

as the initial stress. During these high-stress intervals, the strain rate returned to a similar strain rate to that just prior to the initial stress reduction.

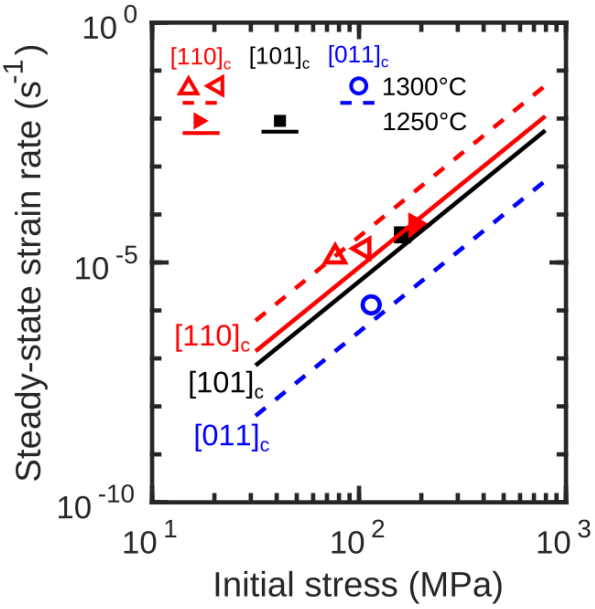

Figure 2: Comparison between strain rates from the steady-state portions of the experiments and published flow laws for single crystals of San Carlos olivine. Symbols represent data from this study (following Table 1), and lines represent flow laws from Bai and Kohlstedt (1992b)**. Color indicates crystal orientation and symbol indicates experiment. Open symbols and dashed lines indicate a temperature of 1300°C, and filled symbols and solid lines indicate a temperature of 1250°C.**

Figure 2 compares the steady-state strain rate from each experiment to predictions of the flow laws for
205 single crystals of San Carlos olivine from Bai and Kohlstedt (1992b). These data are also reported in Table 1. In general, samples loaded in the $[110]_c$, $[101]_c$, and $[011]_c$ orientations exhibit good agreement with the flow-law predictions for olivine deformed at 1250°C and 1300°C. The maximum differences between measured and predicted strain rates are on the order of a factor of 2.3.2 Stress-reduction tests

The results of individual stress-reduction tests are compiled in Figure 3. To obtain these data, we partition each time series of strain into ranges spanning the point just before the stress reduction to the point just before the stress was increased back to the initial stress. The strain at the beginning of this range (i.e., just before the reduction) was set to 0, and the strain data were then corrected for the compliance of the apparatus. This corrected strain after the stress reduction is presented as a function of time in the left column of Figure 3. Small stress reductions result in a small elastic lengthening (negative strain) of the sample that is immediately followed by continued shortening (positive strain). Large stress reductions result in correspondingly large elastic lengthening of the sample, but that lengthening is followed by an additional, time-dependent lengthening of the sample that we refer to as anelastic reverse strain. The period of anelastic lengthening lasts for 10s to 100s of seconds depending on the magnitude of the stress reduction.

We further analyze these data following the method of Blum and Finkel (1982). Many early analyses of stress-reduction experiments (e.g., Ahlquist and Nix, 1971) relied on measuring strain rates after the anelastic reverse strain as a means to assess the “constant microstructure” mechanical behavior. Similar methods have been applied to some geological materials such as ice (Caswell et al., 2015). Unfortunately, strain rates are generally not constant during this increment of stress-reduction tests, and therefore identifying the best segment for calculating a strain rate is not trivial. In contrast, the method of Blum and Finkel (1982) does not rely on measuring strain rates but instead on measuring the magnitude of anelastic reverse strain after the stress reduction and prior to subsequent forward creep. We identify the total amount of reverse strain (both elastic and anelastic) using the minimum strain recorded after the stress reduction. Based on the noise in the strain data, this selection process may overestimate the total reverse strain by ~10^{-4} (roughly 10% of the maximum anelastic reverse strain). We also identify the elastic component of the reverse strain as the strain at the first data point after the reduced stress level is reached.

The total and elastic reverse strains are presented for all experiments in the middle column of Figure 3. For most experiments, the elastic strains are linearly correlated with the magnitude of the stress change and in good agreement with the strains predicted given the Young's modulus in the specific crystal orientation (dashed lines). Agreement with the elastic modulus provides confidence in the apparatus correction and the method of identifying the elastic strain. However, for samples deformed at smaller initial stresses, some elastic strains are smaller than predicted by the elastic modulus, which may indicate the apparatus compliance is overestimated at small loads.

We take the difference between the total reverse strain and the elastic reverse strain to represent the anelastic reverse strain, which is plotted as a function of the magnitude of the stress reduction in the right column of Figure 3. Crystals deformed in the $[110]_c$ and $[101]_c$ orientation exhibit maximum anelastic reverse strains $>10^{-3}$, but significant anelastic reverse strain is only observed following stress reductions greater than ~40% of the initial stress. In contrast, the crystal deformed in the $[011]_c$ orientation exhibits anelastic reverse strains that gradually increase with the magnitude of the stress reduction, even for small stress reductions.

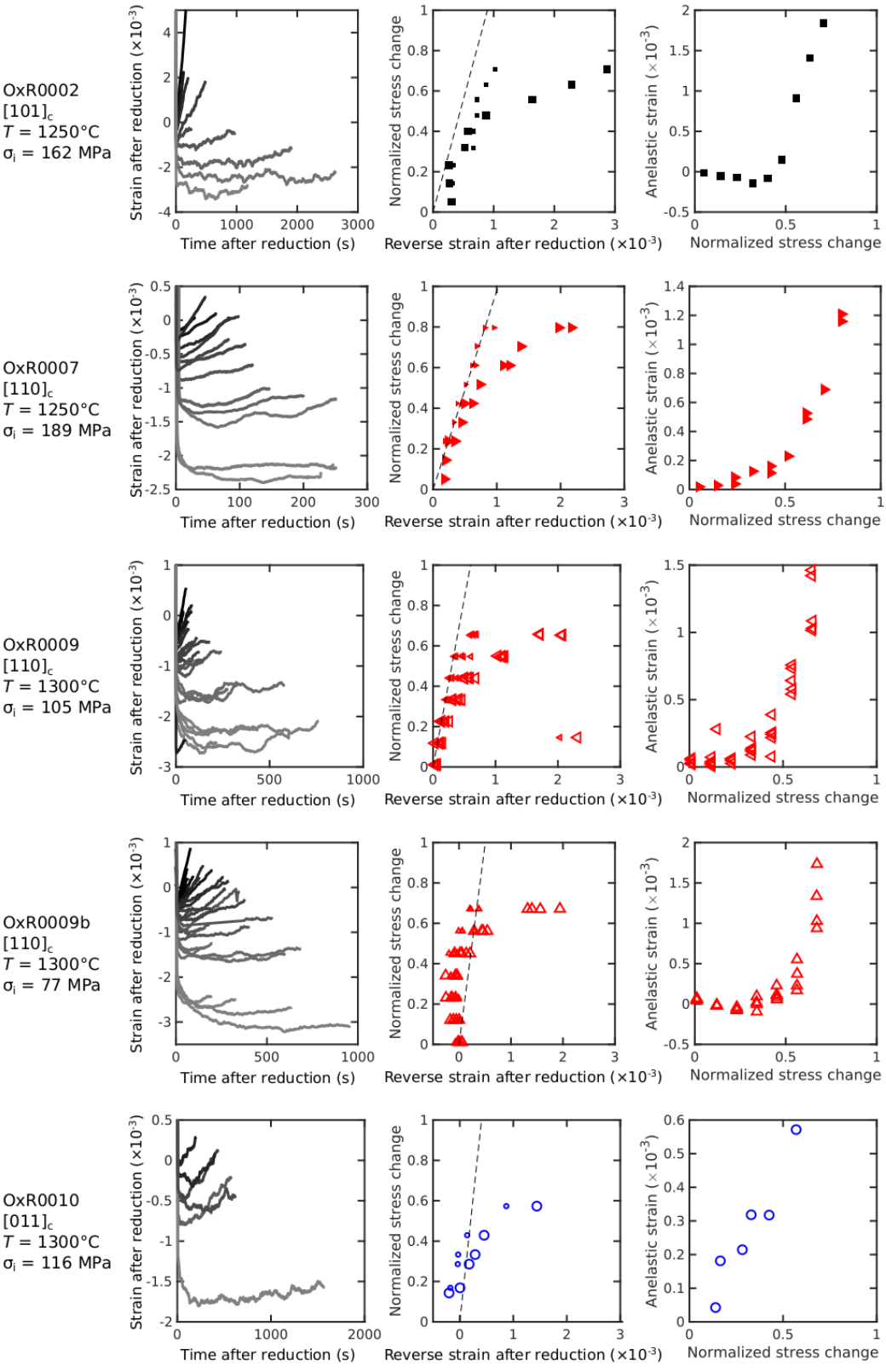
OxR0002
[101]c
T = 1250°C
σi = 162 MPa
OxR0007
[110]c
T = 1250°C
σi = 189 MPa
OxR0009
[110]c
T = 1300°C
σi = 105 MPa
OxR0009b
[110]c
T = 1300°C
σi = 77 MPa
OxR0010
[011]c
T = 1300°C
σi = 116 MPa
Strain after reduction (×10-3)
Time after reduction (s)
Normalized stress change
Reverse strain after reduction (×10-3)
Anelastic strain (×10-3)
Normalized stress change

Figure 3: Compilation of data from all stress-reduction tests. (left) Strains after each reduction are aligned and plotted in grayscale. The grayscale indicates the order of the reductions, with darker colors indicating stress reductions earlier in the experiment. (middle) Magnitude of the stress reduction as a function of the strain after the reduction. Small markers indicate the elastic reverse strain, and larger markers indicate the total reverse strain. The dashed line indicates the Young's modulus for each crystal orientation based on the data of Abramson et al. (1997)**. (right) The anelastic reverse strain as function of the magnitude of the stress reduction. Anelastic reverse strains are calculated as the difference between large markers and small markers in the middle column. Marker shapes and colors are as designated in Table** 1**.**

3.3 Microstructures

Figure 4 presents HR-EBSD maps of sample OxR0009. The dataset collected near the bottom edge of the sample after deformation to 7% strain exhibits lattice rotations dominated by the ω_{12} component. The map of this component exhibits a smooth gradient from the upper-right to lower-left, i.e., in the [100] direction. For the mapped crystal orientation, the ω_{12} component corresponds to rotations around the [001] axis, and large magnitudes of that component are therefore consistent with the presence of (010)[100] edge dislocations (Wallis et al., 2016). Signal in the maps of the ω_{13} and ω_{23} components has magnitudes many times lower than that of ω_{12}, precluding major contributions from other dislocation types to the mapped lattice curvature. The map of shear stress resolved on the (010)[100] slip system (i.e., σ_{ab}) also exhibits gradients in the [100] direction, varying by magnitudes on the order of 100 MPa over distances of a few hundred microns. The dataset collected from near the centre of the sample at the final strain of 38% exhibits lattice rotations similar to those in the dataset collected at lower strain. The stress distribution is homogeneous over the length scale of the map, which is notably smaller than that collected at 7% strain. However, the dataset collected near a side edge of the sample at 38% strain exhibits more discontinuous rotation and stress fields. Each component of the lattice rotation exhibits two linear discontinuities corresponding to subgrain boundaries. The boundaries have traces parallel to [010] and are most pronounced in the map of ω_{12}, consistent with them being dominated by (010)[100] edge dislocations. The boundaries also coincide with discontinuities in the map of σ_{ab}. These stresses have the

greatest magnitudes, i.e., are localised, adjacent to the boundaries. Across the boundaries, the stresses exhibit changes in sign and changes in magnitude on the order of 100 MPa. The orientation gradients between the upper-right and lower-left corners of each map of ω_{12} correspond to average GND densities in the range $4x10^{11}$ m^{-2} to $8x10^{11}$ m^{-2} (Wallis et al., 2016).

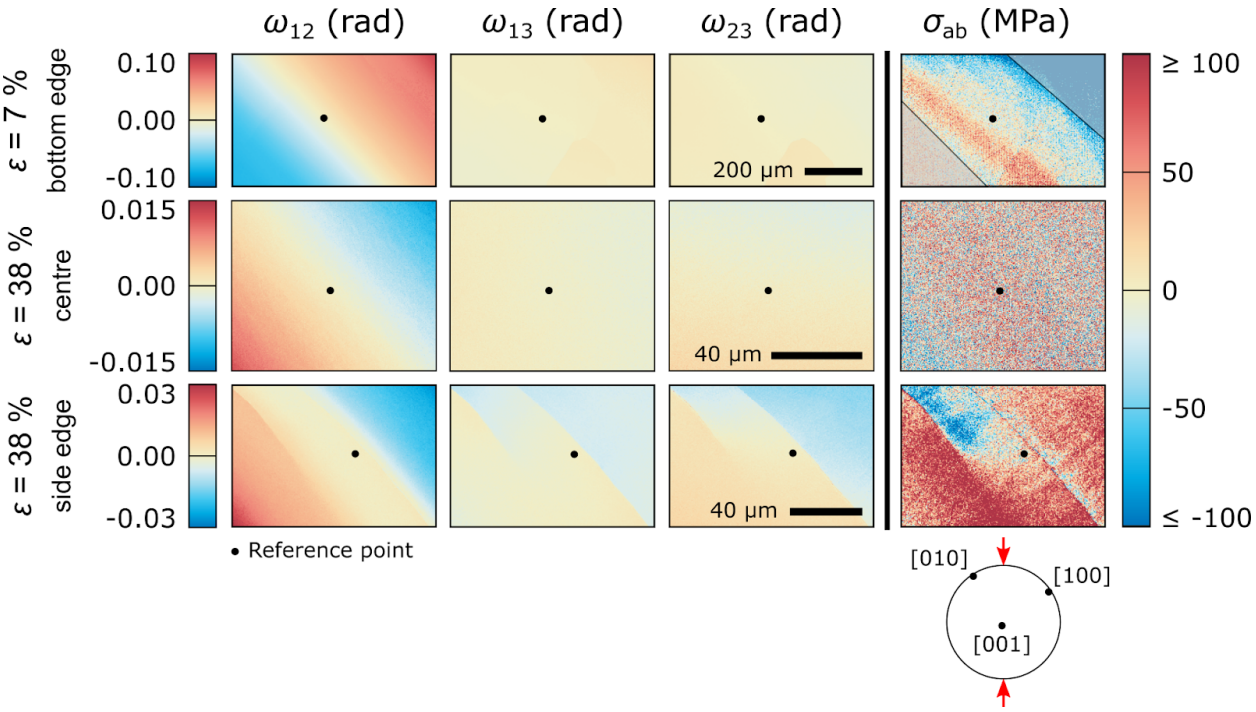

Figure 4: HR-EBSD maps of sample OxR0009, which was compressed in the $[110]_c$ orientation indicated in the pole figure, at different strains and locations in the sample annotated on the left. Lattice rotations (ω_{ij}) and shear stress on the (010)[100] slip system (σ_{ab}) are relative to the orientation and stress state, respectively, of the reference points marked in black. The greyed-out areas in the top stress map indicate regions where the stress measurements are unreliable due to the large distances and large lattice rotations relative to the reference point.

4 Discussion

In this study we present results of stress-reduction tests carried out on single crystals of San Carlos olivine. The key observations are: 1) prior to stress reductions, strain rates reach a steady state in agreement with previously published flow laws for olivine, 2) after stress reductions of sufficient

magnitude, an anelastic reverse strain is observed, 3) the magnitude and duration of anelastic reverse strain is a strong function of the magnitude of the stress reduction, 4) significant heterogeneity in the residual stress is correlated with gradients in lattice orientation (i.e., with GNDs). To interpret these observations, we first compare previously published interpretations of stress reduction tests to our data and then reanalyze our data in the context of recent work on the plastic deformation of olivine.

4.1 Comparison to previous interpretations of stress-reduction tests

Stress-reduction tests have been a common technique for investigating the microphysics of creeping, crystalline materials. Two primary aspects of the microphysics have been investigated with stress reduction tests. The first is the concept of a backstress (or internal stress), which is related to the details of the microstructural evolution during deformation. The observation of backstress in single crystals indicates that it arises from the long-range elastic interactions among lattice dislocations. Specifically, for the average backstress within a crystal to be non zero requires, by definition, heterogeneity in the microscopic distributions of stresses (e.g., Gibeling and Nix, 1981). The creep rate is assumed to result from the action of an effective stress, σ_e, which is the difference between the externally applied stress and the backstress, $\sigma_e = \sigma - \sigma_b$, where σ is the former and σ_b is the latter. Forward creep results from positive values of σ_e, and reverse creep results from negative values of σ_e.

Early experiments on pure metals by Gibbs (1966), solid-solution alloys by Ahlquist and Nix (1971), and ionic crystals by Menezes and Nix (1971) demonstrated that the average backstress could be determined with stress-reduction tests (for a review, see Takeuchi and Argon, 1976). In this method, the microstructure and associated σ_b are presumed to remain constant during the nearly instantaneous stress reduction. Just after the reduction, the immediate strain rate is observed to be positive, negative, or approximately zero, depending on the magnitude of the stress reduction. These scenarios are presumed to indicate that the applied stress after the reduction is either greater than, less than, or equal to the

backstress, respectively. Therefore, the reduced stress at which the subsequent strain rate is approximately zero is taken to be equal to the backstress. However, there is some controversy about the practical aspects of identifying a zero strain rate (for a review, see Nix and Ilschner, 1979), and therefore we adopt the method of Blum and Finkel (1982), as described above. In this latter method, the reduced stress at which anelastic reverse strain becomes measurable is taken as equal to the average backstress.

These methods have been used to characterize backstresses in a wide range of materials. Two well-cited studies, in particular, had remarkably consistent results, estimating backstresses at 52% of the initial stress in both pure metals (Evans et al., 1985) and solid-solution alloys (Blum and Finkel, 1982). Many subsequent modeling efforts therefore have taken this value as a constant in the creep of metals (e.g., Biberger and Gibeling, 1995). Similar values have been observed in some ceramics such as $Gd_3Ga_5O_{12}$ (Wang et al., 1996), which exhibited a backstress of 62% of the initial stress. However, broader compilations of backstress estimates (Argon and Takeuchi, 1981; Čadek, 1987; Milička et al., 2007; Takeuchi and Argon, 1976) demonstrate that the relationship between the backstress and initial stress varies systematically as a function of the initial stress. For instance, Menezes and Nix (1971) reported values of the backstress in LiF that vary systematically between 21% and 83%. In addition, Wang et al. (1993) reported backstresses in $SrTiO_3$ up to ~100%.

The second aspect of the microphysics of creep investigated with stress reduction tests is the rate limiting process at constant microstructure. As noted above, the specific dislocation arrangements are considered to be unchanged (neglecting unbowing of dislocations) during the stress reduction. Therefore, in the case that the stress reduction is small and no anelastic strain occurs, the forward strain rate just after the reduction is a function of the same microstructure as before the reduction. A variety of studies (for a review, see Biberger and Gibeling, 1995) have evaluated these types of tests and found that the strain rates after a stress reduction are fit well by a flow law with an exponential dependence of strain rate on the

stress, which is a form typically used to describe plastic deformation limited by the glide velocity of dislocations (e.g., Kocks et al., 1975). Furthermore, the dependence of the strain rate on the reduced stress can be related to the apparent activation area of gliding dislocations (the area of slip plane traversed in a single activation event), which was shown to have a direct relationship to the observed spacing of free dislocations in subgrain interiors. These results led the authors (and authors cited therein) to conclude that the strain rates directly after a load reduction are dominated by the kinetics of gliding dislocations. Similar conclusions based on stress-reduction tests have been drawn for LiF (Müller et al., 1992), SrTiO3 (Wang et al., 1993), and $Gd_3Ga_5O_{12}$ (Wang et al., 1996).

The observations described above have played a large part in informing the development of composite models to describe both transient and steady-state creep properties of crystalline materials. Key early models include those proposed by Hart (1976), Nix and Ilschner (1979), and Mughrabi (1980), although a variety of elaborations have been proposed (Bammann, 1989; Garmestani et al., 2001; e.g., Korhonen et al., 1987). The key features of these models are that 1) plastic deformation across a wide range of conditions is effectively controlled by the glide of dislocations, 2) the glide velocity of those dislocations is moderated by the long-range stresses associated with heterogeneity in the state variables that describe the microstructure (what we refer to as a backstress), and 3) the macroscopic behavior can be modified by different recovery mechanisms (such as dislocation climb and annihilation) that modify the backstress. We use these three concepts as a foundation for analyzing our data for olivine in the next section.

4.2 Linking stress reductions at elevated temperatures to low-temperature plasticity in olivine

Our working hypothesis based on the discussion above is that deformation after a stress reduction is controlled by the glide of dislocations, and the anelasticity observed after larger stress reductions is

controlled by average backstresses associated with the long-range interactions of dislocations. Plastic deformation and the evolution of backstresses in the glide-controlled regime (often referred to as low-temperature plasticity) was recently investigated for olivine by Hansen et al. (2019). In that work, the authors used experiments conducted at temperatures as a low as room temperature to examine the yield strength and hardening behavior of single crystals and polycrystalline samples of San Carlos olivine. Notably, the hardening behavior of single crystals is indistinguishable from the hardening behavior of polycrystalline aggregates, which we interpret to indicate that the dominant processes leading to strain hardening are intragranular. Furthermore, they observed a distinct Bauschinger effect, which supports the conclusion that the hardening is associated with long-range interactions of dislocations (see section 2.5 in Kassner, 2015). This conclusion is further supported by microstructural correlations of the GND density field with residual stress fields in the same samples (Wallis et al., 2020a). In support of the hypothesis that these long-range stress fields are also important during deformation at high temperatures, we see spatial correlations between lattice rotation gradients (i.e., GND densities) and stresses in our samples (Figure 4) and the similar samples of Wallis et al. (2017). Furthermore, Wallis et al. (2020b) highlighted the similarities between stress fields in aggregates of olivine deformed at temperatures of 1150–1250°C and those deformed at room temperature. These similarities include the magnitudes, the forms of the probability distributions, and the characteristic length scales of the stress heterogeneity, along with a causative link to GNDs in both temperature regimes.

4.2.1 Magnitude of anelastic reverse strain

To further analyze these data, we assess the magnitude of anelastic reverse strain after a stress reduction. We use the equations describing plasticity in olivine outlined by Hansen et al. (2019). We consider a flow law for the plastic strain rate from gliding dislocations, $\dot{\varepsilon}_{\mathrm{p}}$, of the form

$$\dot{\varepsilon}_{\mathrm{p}} = A_1 \exp\left(-\frac{\Delta F}{\mathrm{R}T}\right) \sinh\left(\frac{\Delta F}{\mathrm{R}T}\frac{\sigma - \sigma_{\mathrm{b}}}{\Sigma}\right), \tag{1}$$

where A_1 is a constant with units of s^{-1}, $\triangle F$ is the activation energy, R is the gas constant, T is the temperature, σ is the applied stress, σ_b is the backstress, and Σ is the effective lattice friction. As described above, the effective stress ($\sigma - \sigma_b$) determines the glide velocity of dislocations, and therefore any evolution of the strain rate during a test at constant stress results from the evolution of σ_b. It is important to note that $\dot{\varepsilon}_{\mathrm{p}}$ will be negative if $\sigma_b > \sigma$. Hansen et al. (2019) provided an evolution equation for σ_b,

$$\frac{\mathrm{d}\sigma_{\mathrm{b}}}{\mathrm{d}\varepsilon_{\mathrm{p}}} = \gamma\left[\sigma_{\mathrm{b,max}} - \mathrm{sgn}\left(\dot{\varepsilon}_{\mathrm{p}}\right)\sigma_{\mathrm{b}}\right], \tag{2}$$

where γ is a rate constant and $\sigma_{b,max}$ is the maximum backstress. Although they implemented this equation in an empirical manner, there are physical meanings to each of these terms (e.g., Mecking and Kocks, 1981). Assuming the backstress is related to the dislocation density (e.g., Taylor, 1934), $\gamma\sigma_{b,max}$ is related to the dislocation nucleation rate, and γ is related to the dislocation recovery rate associated with dynamic recovery. The explicit links between backstress evolution and dislocation density in olivine will be explored in future work.

An analytical solution exists for equation 2, providing the evolution of the back stress as a function of strain,

$$\sigma_{\mathrm{b}}(\varepsilon_{\mathrm{p}}) = \mathrm{sgn}\left(\dot{\varepsilon}_{\mathrm{p}}\right)\sigma_{\mathrm{b,max}} + \left(\sigma_{\mathrm{b,0}} - \mathrm{sgn}\left(\dot{\varepsilon}_{\mathrm{p}}\right)\sigma_{\mathrm{b,max}}\right)\exp\left(-\gamma\varepsilon_{\mathrm{p}}\mathrm{sgn}\left(\dot{\varepsilon}_{\mathrm{p}}\right)\right), \tag{3}$$

where $\sigma_{b,0}$ is the initial back stress. This equation can be rearranged to predict the total plastic strain necessary for σ_b to reach a final value, $\sigma_{b,f}$,

$$\varepsilon_{\mathrm{p}} = \left[\mathrm{sgn}\left(\dot{\varepsilon}_{\mathrm{p}}\right)\gamma\right]^{-1} \ln\left[\frac{\sigma_{\mathrm{b,f}} - \mathrm{sgn}\left(\dot{\varepsilon}_{\mathrm{p}}\right)\sigma_{\mathrm{b,max}}}{\sigma_{\mathrm{b,0}} - \mathrm{sgn}\left(\dot{\varepsilon}_{\mathrm{p}}\right)\sigma_{\mathrm{b,max}}}\right]. \tag{4}$$

In the case of a large stress-reduction test, $\dot{\varepsilon}_p < 0$ just after the reduction. The backstress at the time of the reduction, $\sigma_{b,0}$, is some fraction, β, of the initial applied stress prior to the reduction, σ_i. After the reduction, the backstress will decrease until a value of $\sigma_{b,f}$ is reached. This final value cannot, by definition, be larger than the applied stress after the reduction, σ_r, and it will only reduce further than σ_r if some additional recovery process is involved, such as "static" annealing of the dislocation density (e.g., annihilation by dislocation climb). Based on published static annealing rates for dislocations in olivine (Karato et al., 1993; Toriumi and Karato, 1978), estimates for the total recovery for the longest durations of anelastic strain (100s of seconds) range from <1% to ~10%. Therefore, we assume that static recovery is negligible during the anelastic portion of these experiments, and we expect that $\sigma_{b,f} = \sigma_r$ at the end of anelasticity and prior to subsequent forward creep. These considerations allow us to rewrite equation 4 for the maximum anelastic reverse strain after a stress reduction as

$$\varepsilon_p = -\frac{1}{\gamma}\ln\left(\frac{\sigma_r + \sigma_{b,max}}{\beta\sigma_i + \sigma_{b,max}}\right). \quad (5)$$

Note that the assumption made above is only valid for the case in which anelastic reverse strain occurs (i.e., when $\sigma_r < \beta\sigma_i$). If the applied stress is not reduced below this threshold, then no anelastic reverse strain occurs (i.e., $\varepsilon_p = 0$).

Equation 5 can be compared to our experimental data to find values for key parameters. We assume that $\sigma_{b,max}$ = 1.8 GPa according to the results of our experiments at low temperatures (Hansen et al., 2019). We then compare the measured anelastic reverse strains for large stress reductions to equation 5 to find the best-fit values of γ and β (and therefore the backstress prior to the stress reduction from equation 4). Values for these parameters are presented in Table 1 and a comparison of equation 5 to anelastic reverse strains is presented in Figure 5.

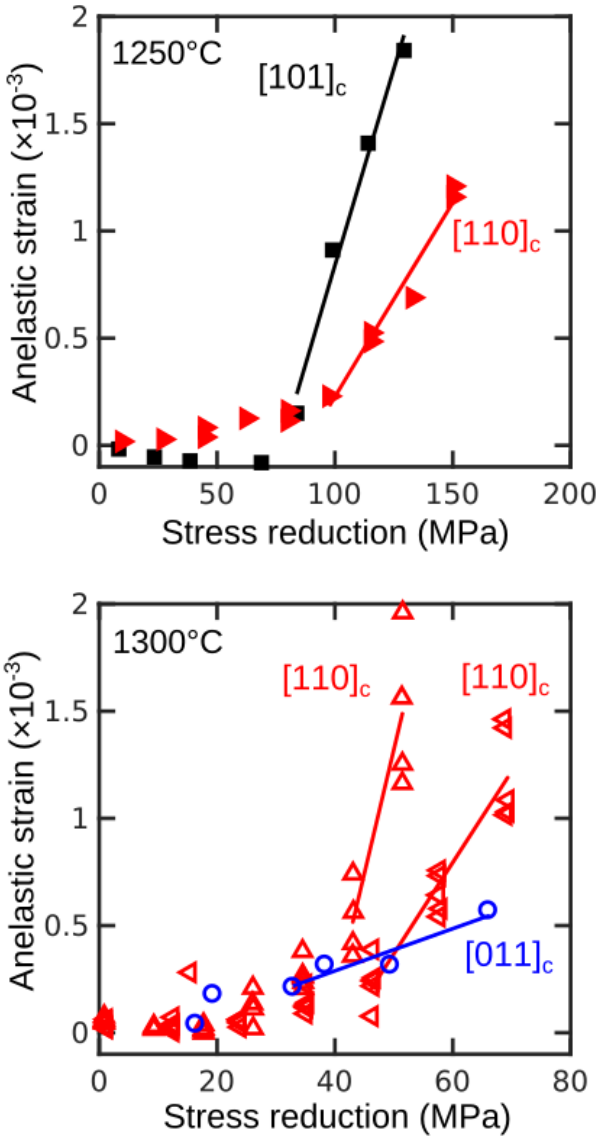

Figure 5: Anelastic reverse strain as a function of the magnitude of the stress reduction at two different temperatures. Marker shapes and colors are as designated in Table 1**. Solid lines are fits to equation** 5**. Only data with clearly measurable anelastic reverse strain are included in fits.**

These results indicate that, in olivine deformed in the $[110]_c$ and $[101]_c$ orientations, the magnitudes of anelastic reverse strain are consistent with backstresses between 48 and 61% of the initially applied stress, which are largely consistent with most previously reported values in other materials (see section 4.1

above). Interestingly, our results for olivine deformed in the $[011]_c$ orientation suggest that the backstress is nearly equal to the applied stress. This difference in backstress between different crystal orientations, and therefore between different activated slip systems, is likely a result of different rates of dislocation recovery, as will be explored later in this section.

The values of the best-fit rate constant, γ, also differ between crystal orientations. Olivine deformed in the $[110]_c$ and $[101]_c$ orientations is characterized by values of γ between 5 and 28. However, olivine deformed in the $[011]_c$ orientation is characterized by a value of γ of 55. The former values are considerably smaller than the value of $\gamma = 75 \pm 20$ determined in low-temperature experiments (Hansen et al., 2019). However, the value of $\gamma = 55$ for the crystal deformed in the $[011]_c$ orientation is within error of that determined in previous experiments. Those previous experiments examined both polycrystalline aggregates and single crystals, but only single crystals in the $[011]_c$ and $[111]_c$ orientations were investigated, and both orientations should have a large part of the dislocation content on the (010)[001] slip system. Therefore, at least where comparisons can be made, this analysis of the anelastic reverse strain is consistent with the same mechanism of deformation being responsible for transient deformation at low and high temperatures, as suggested by the microstructural interpretations of Wallis et al. (2020b). Furthermore, these results provide initial evidence that transient deformation on the strongest slip system may dominate the transient response of a polycrystalline sample, which is inconsistent with some recent theoretical treatments of transient creep in olivine suggesting the transient is controlled by the weakest slip system (Masuti et al., 2019).

4.2.2 Strain rates immediately after a stress change

If the low-temperature plasticity flow law can explain the magnitude of the anelastic reverse strain, then following from previous treatments for metals (e.g., Biberger and Gibeling, 1995), we expect the same flow law can explain the strain rates observed just after a change in stress. This hypothesis is similar to

the suggestion by Cooper et al. (2016) that load relaxation experiments on olivine single crystals are rate limited by the glide of dislocations. We plot strain rates just after our stress reductions in Figure 6a as a function of the effective stress, σ_e, which was determined by subtracting the value of σ_b determined in Figure 5 from the reduced stress. In other words, we suggest these stresses and strain rates in Figure 6a reflect the rheological behavior of olivine when no backstress is present. Only strain rates for small stress reductions without any measurable anelastic reverse strain are presented. Strain rates from the crystal deformed in the $[011]_c$ direction are not plotted because all tests for that sample exhibit some anelasticity. The observed strain rates are consistently faster than the strain rates predicted for steady-state creep, and interestingly, the apparent power-law exponent is ~1. This observation may initially seem at odds with the hypothesis that creep at "constant microstructure" is controlled by the glide of dislocations. However, as recently discussed in the context of olivine deformation by Cooper et al. (2016), the apparent stress exponent of an exponential flow law decreases with decreasing stress, and therefore, these data could indeed be explained by an exponential function. In fact, the sinh function employed by Hansen et al. (2019) following the canonical work of Garofalo (1963) and described in equation 1 results in a linear relationship between strain rate and stress at low stresses.

We also compare these strain rates to data from previously published experiments at high temperatures in Figure 6b. To do so, we need data from experiments in which the backstress, and therefore the effective stress, is known. We suggest that the strain rates just after initial loading of constant-stress experiments reasonably represent a case in which the backstress is zero since no strain has accumulated to produce a backstress. Data of this type are available for single crystals of San Carlos olivine (Cooper et al., 2016; Hanson and Spetzler, 1994) and polycrystalline aggregates of San Carlos olivine (Chopra, 1997). We also include the yield stresses from single crystals deformed at room temperature at constant strain rate (Hansen et al., 2019). A complication in comparing data from the first increments of strain in constant-stress (or constant-strain-rate) tests is that the initial strain rate (or stress) is likely highly

455 sensitive to the density of mobile dislocations present in the starting material. Therefore, we normalize the strain rates in Figure 6b by the dislocation density at the beginning of the measurement. For our data, the initial dislocation density is calculated from the initial stress before the reduction using the dislocation-density piezometer of Bai and Kohlstedt (1992a). The initial values of dislocation density in the previous studies noted above are not available, but we estimate the starting density of single-crystal 460 samples as 10^{10} m^{-2} based on observations in untreated San Carlos olivine (Toriumi and Karato, 1978) and of polycrystalline samples as 10^{12} m^{-2} based on observations of hot-pressed Anita Bay dunite (Karato et al., 1986).

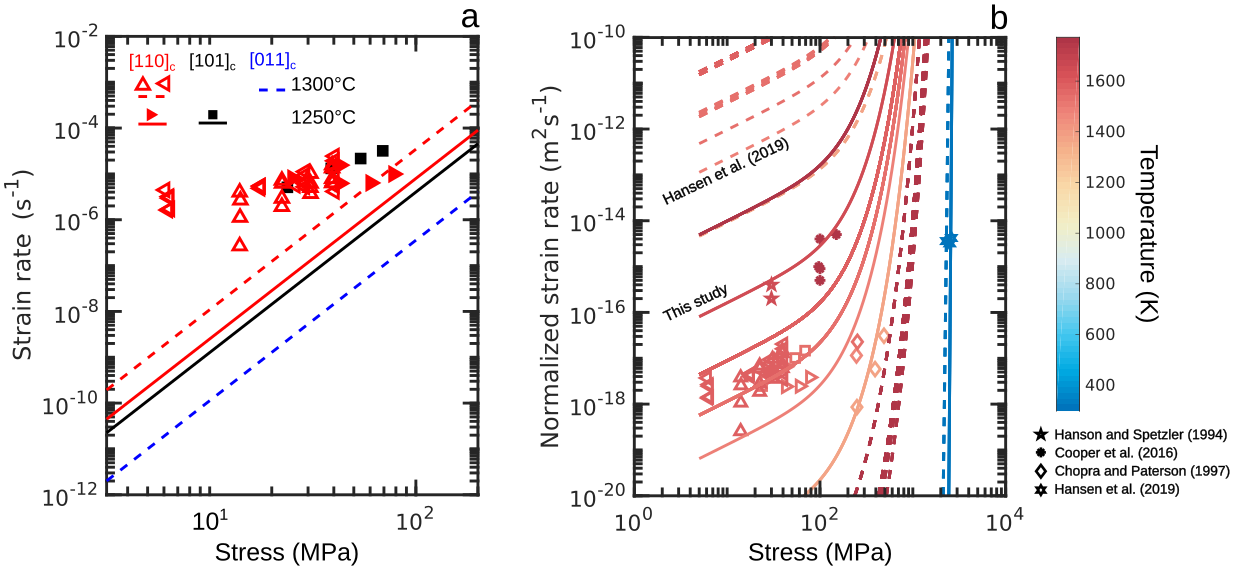

Figure 6: Analysis of strain rates measured immediately after stress reductions. (a) Strain rates measured after small reductions for which no anelastic reverse strain was detected. Stresses are effective stresses, that is, the applied stress minus the measured backstress given in Table 1**. Marker shapes and colors are as designated in Table** 1**. Dashed and solid lines are flow laws for single crystals of olivine from Bai et al.** (1991)**. (b) Strain rates as in (a) compared to previously published data. Strain rates from previous high-temperature creep tests** (Chopra, 1997; Cooper et al., 2016; Hanson and Spetzler, 1994) **were taken from the beginning of experiments in which the backstress is expected to be negligible. Data from Hansen et al.** (2019) **are yield stresses measured in constant-strain-rate experiments. Dashed lines represent the flow law from Hansen et al.** (2019)**. Solid lines represent the flow law calibrated in this study.**

The comparison in Figure 6b provides two key observations. First, the apparent stress exponent differs for each individual data set, systematically increasing with increasing stress. This observation is consistent with deformation just after a stress reduction being controlled by the glide of dislocations following an exponential or sinh flow law. Second, we also plot the low-temperature plasticity flow law from Hansen et al. (2019) (dashed lines in Figure 6b). This flow law does well at predicting the strain rates in the room-temperature experiments on which the flow law is based, but does poorly at predicting the strain rates at high temperatures. The plasticity flow law overpredicts strain rates from this study by approximately six orders of magnitude. This discrepancy at high temperatures is not that surprising since the temperature-dependence is the most poorly constrained component of the flow law. Not only was the flow law primarily calibrated with data collected at room temperature, but data at higher temperatures were either subject to low resolution in temperature measurement or were taken from other studies conducted with different methods. Therefore, we suggest that (1) our data are consistent with transient deformation being controlled by the process of dislocation glide but that (2) existing flow laws for glide-controlled plasticity in olivine need to be recalibrated before extension to such high temperatures.

4.2.3 Recalibration of the low-temperature plasticity flow law

Here we recalibrate the flow law for low-temperature plasticity in olivine using the data presented in Figure 6b. This data set covers a temperature range from 20° to 1300°, and therefore “low-temperature plasticity” is somewhat of a misnomer. To be clear, by “low-temperature plasticity” we are specifically referring to a regime in which the strain rate is controlled by the glide velocity of dislocations, as in equation 1, regardless of the temperature. However, we must modify equation 1 to reasonably apply this flow law to the range of data in Figure 6b. Although the form of the flow law calibrated by Hansen et al. (2019) was derived from the Orowan equation (see their equation 6), the density of mobile dislocations that actually produce strain was assumed to be relatively constant and therefore was incorporated into A_1.

This assumption is generally justified for applications to low-temperature, high-stress deformation because the stress dependence of the sinh term far outweighs the stress dependence of the mobile dislocation density. However, this is not necessarily the case at high temperatures, and therefore we suggest a more robust form of the low-temperature plasticity flow law as

$$\dot{\varepsilon}_{\mathrm{p}} = A_2 \rho \exp\left(-\frac{\Delta F}{\mathrm{R}T}\right) \sinh\left(\frac{\Delta F}{\mathrm{R}T}\frac{\sigma - \sigma_{\mathrm{b}}}{\Sigma}\right), \tag{6}$$

where A_2 is a constant and ρ is the density of mobile dislocations.

Figure 6b compares our compiled data for strain rates controlled by dislocation glide to a best fit to equation 6. In the applied fitting procedure, we fixed Σ = 3.1 GPa, which is well constrained by the previous calibration using low-temperature data, and conducted a grid search to find the optimum values of A_2 and ΔF. The best-fit values of these parameters are $A_2 = 10^{11.1\pm0.2}$ m^2s^{-1} and ΔF = 827±20 kJ/mol. This calibrated flow law is able to capture the observed behavior over a wide range in temperatures, reasonably predicting both the magnitudes of the strain rates as well as the change in the apparent stress exponent as a function of temperature. Furthermore, combining equation 6 with a parameterization of the backstress evolution, such as that in equation 2, allows the complete transient to be predicted. Different values of γ can be used to predict the transient behavior of different slip systems, as discussed in relation to Figure 5. However, we note that the dislocation recovery mechanisms implicit in equation 2 are only calibrated for use at low temperatures. Therefore, prediction of the steady-state strain rates at elevated temperatures requires high-temperature recovery mechanisms to be accounted for. Incorporating these recovery mechanisms into a parameterization of dislocation creep in olivine will be a key topic addressed in future work.

We can, however, assess the magnitude of the backstresses at high temperature. To restate the discussion above, we suggest that equation 6 controls the macroscopic strain rate in both transient and steady-state

creep, and the evolution between the two regimes reflects the evolution of the backstress. In this framework, at steady state, the steady-state strain rate would be equal to equation 6, which allows us to solve for the backstress at steady state,

$$\sigma_{\mathrm{b}} = \sigma - \operatorname{asinh}\left[\frac{\dot{\varepsilon}_{\mathrm{ss}}}{A_2\rho}\exp\left(\frac{F}{\mathrm{R}T}\right)\right]\frac{\mathrm{R}T\Sigma}{F}, \tag{7}$$

where $\dot{\varepsilon}_{\mathrm{ss}}$ is the steady-state strain rate. In Figure 7, we present values of the steady-state back stress estimated with equation 7. These values were calculated using steady-state strain rates predicted by the flow laws for single-crystal olivine from Bai and Kohlstedt (1992b) and dislocation densities predicted by the dislocation-density piezometer from Bai and Kohlstedt (1992a). These calculated backstresses compare favorably to those observed in stress-reduction tests, which provides further confidence in our calibration of equation 6 and in our suggestion that equation 6 can be used to predict the steady-state strain rate if the backstress is known.

Notably, the calculated curves in Figure 7 capture the orientation dependence of the backstress. Equation 7 correctly predicts that crystals compressed along $[011]_c$ have a backstress nearly equal to the applied stress, and that crystals deformed in other orientations have a backstress that is approximately 50% of the applied stress. Because we use the same values of A_2, F, and Σ regardless of orientation, the orientation dependence of the calculated backstress results entirely from the different steady-state flow laws. Therefore, there is a clear link between the anisotropy of the steady-state creep rate and the anisotropy of the backstress evolution, which we suggest is primarily a reflection of anisotropic rates of dislocation recovery (e.g., Wang et al., 2016). We reiterate that, although we propose dislocation creep during the transient and steady state is governed by equation 6, the steady-state strain rate can still be set by the rates of dislocation climb that counteract the buildup of additional backstress.

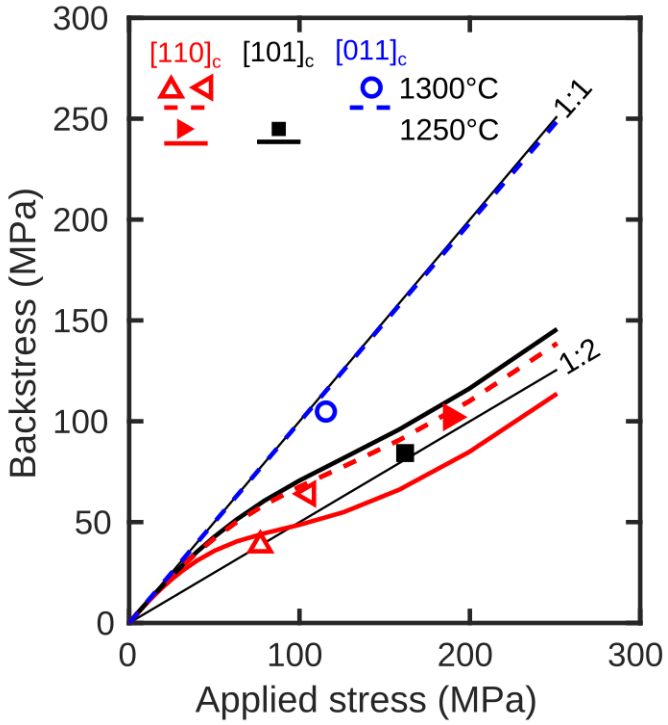

Figure 7: Measured and predicted backstresses as a function of the applied stress. Markers indicate backstresses determined using the analysis presented in Figure 5**. The two thin black lines are guides for values of backstress equal to the applied stress (1:1) or half of the applied stress (1:2). The curves are backstresses predicted from equation** 7**.**

4.2.4 Implications for the type of transient creep and load relaxation

Our hypothesis linking low-temperature plasticity, transient creep, steady-state creep, and the evolution of backstress predicts several other phenomena. A key phenomenon is variation in the sign of the strain acceleration during the transient. That is, whether or not the strain rate decreases (a “normal” transient) or increases (an “inverse” transient) during the evolution to steady state. Hanson and Spetzler (1994) observed that the type of transient depends on the crystal orientation, and Cooper et al. (2016) observed a transition in the type of transient in the same experiment as the applied stress was increased in steps. Figure 8a schematically describes how the model presented here can predict both types of transients. We

suggest that the strain rates for olivine will generally be described by the low-temperature plasticity flow law (equation 6). After initial application of stress to the sample, the mobile dislocation density and backstress evolve toward their steady-state values. This change in the microstructural parameters shifts the low-temperature plasticity flow law to higher or lower strain rates until the strain rate matches the apparent steady-state power law. At the onset of deformation, if the low-temperature plasticity flow law predicts faster strain rates than the steady-state strain rate, then the initial strain rate will be fast, and the flow law will gradually shift to slower rates (a normal transient) due to an increasing backstress. Conversely, if the initial strain rate dictated by the flow law is slower than at steady-state, the flow law will shift to faster rates (an inverse transient) due to an increase in the density of mobile dislocations. Therefore, we suggest that the intersection of the low-temperature plasticity flow law and the steady-state power law can be used to predict whether normal or inverse transients will occur. Figure 8b presents the type of transient predicted by this method over a range of temperatures and pressures for all three orientations of olivine. The predictions are in excellent agreement with observations in this study (Table 1), as well as with the observations made by Hanson and Spetzler (1994) and Cooper et al. (2016) .

We additionally note that, while this analysis correctly predicts a normal transient for the initial loading of olivine along $[011]_c$, it also predicts that once steady state is reached, any subsequent stress increase would lead to an inverse transient. Therefore, this model also correctly predicts the change in the type of transient from normal to inverse observed by Cooper et al. (2016) in progressive load-stepping experiments (see their Figure 4a).

We finally point out that our model is similar to that developed by Stone (1991) (in turn, fundamentally based on the theory of Hart (1970)) and applied to geological materials such as halite (Stone et al., 2004) and olivine (Cooper et al., 2016). The “master curve” described by that model is essentially represented here by the low-temperature plasticity flow law, for which shifts of the master curve occur due to changes

in the backstress. The difference lies in the fact that the master curve of Stone (1991) represents a plastic yield stress controlled by the subgrain size in combination with a flow law describing Nabarro-Herring creep among subgrains. In that formulation, shifts of the master curve occur due to changes in the subgrain size. The transition of Stone's master curve to Nabarro-Herring creep at low stresses was inspired by strain rates during load relaxation that approached a linear relationship with stress. We emphasize that the same phenomenological response is present in our model due to the sinh term in the low-temperature plasticity flow law. The model of Stone (1991) explains load-relaxation data for halite exceptionally well (Stone et al., 2004), collapsing the data set to a master curve when scaled by the subgrain size. In contrast, in load relaxation experiments on single crystals of olivine in the $[011]_c$ orientation, Cooper et al. (2016) found that the master curve is not shifted by the subgrain size. In fact, they demonstrated that the load-relaxation response is unchanged by the initially applied stress and any associated changes in microstructure, always falling on the same stress-strain-rate curve. Therefore, Cooper et al. (2016) suggested that a different physical process controls the relaxation response of olivine, dislocation glide limited by the Peierls stress.

Our data and analysis provides an alternative, but related, explanation that can be applied to both halite and olivine. As noted above, we suggest the backstress controls shifts in the low-temperature plasticity flow law. Figure 7 illustrates that the backstress for crystals deformed in the $[011]_c$ orientation is essentially equal to the applied stress. This observation suggests that, during the initial evolution to steady state, the backstress reaches a value equal to the applied stress before the low-temperature plasticity flow law can shift to lower rates to reach the steady-state rate. Therefore, during a load relaxation experiment, the effective stress is initially zero, and forward strain only proceeds due to the reduction of the backstress associated with dislocation recovery. Continued forward strain and reduction of backstress would occur in lock step and simply follow the steady-state power law regardless of the initial stress, which is consistent with the observation of Cooper et al. (2016). In contrast, for halite (Gupta and Li, 1970) and other

orientations of olivine (Figure 7), the backstresses are a smaller portion of the applied stress, and therefore the effective stress is both finite and a function of the applied stress. In this context, a stress relaxation
585 experiment would follow the low-temperature plasticity flow law prior to any relaxation of the backstress. Therefore, we predict that stress relaxation experiments conducted on other orientations of olivine would exhibit a similar response as halite, following the low-temperature plasticity flow law and dependent on the magnitude of the initial stress.

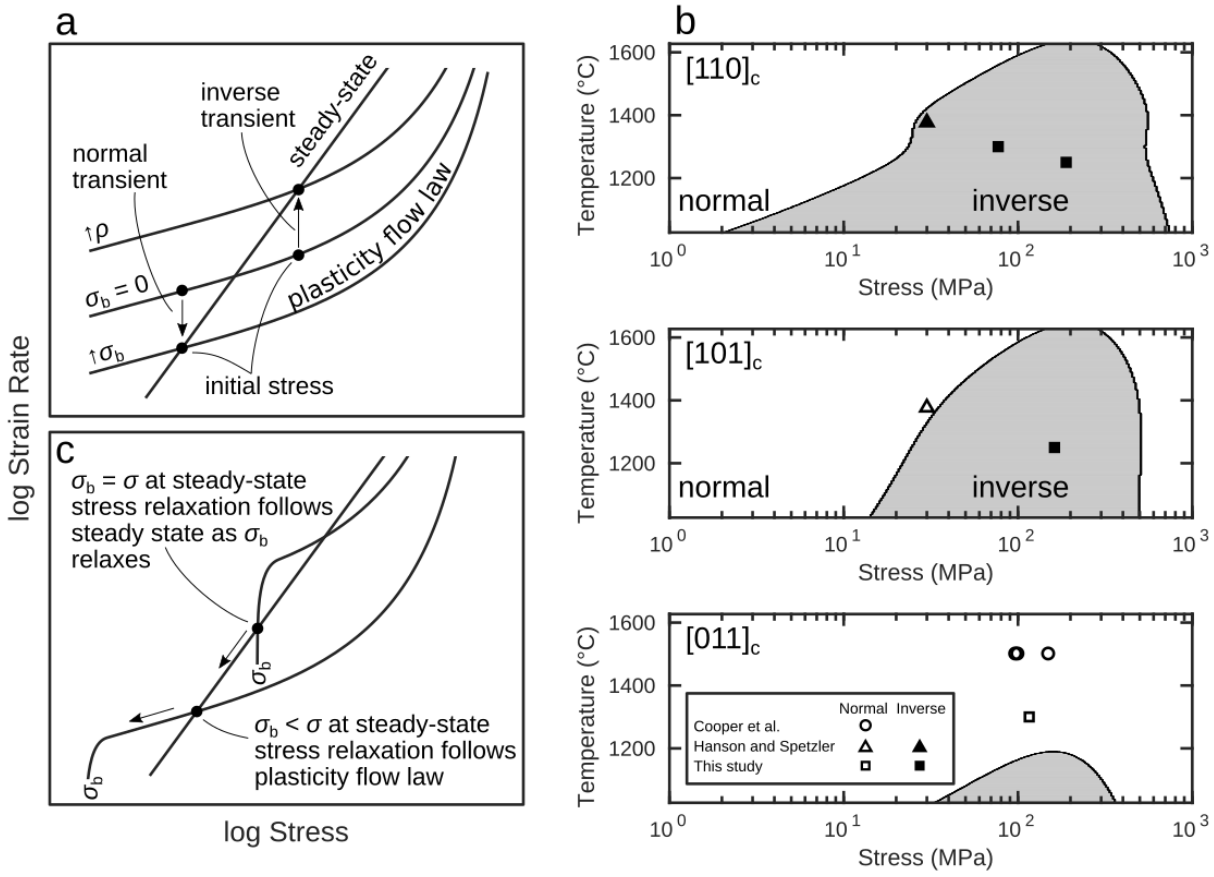

Figure 8: Evaluation of the proposed model in the contexts of the shape of the transient and of stress relaxation. (a) Schematic description of our model. The initial stress applied to a sample leads to a strain rate controlled by the low-temperature plasticity flow law without any backstress. If this strain rate is higher than the steady-state strain rate, we predict that the transient will be normal and controlled by the increase in backstress. If this strain rate is lower than the steady-state strain rate, we predict that the transient will be inverse and controlled by the increase in density of mobile dislocations. In this schematic, the backstress is assumed to always be less than the minimum stress on the plot. (b) Conditions leading to inverse or normal transients calculated with the concept presented in (a). Data for comparison come from the initial strain rates at the start of experiments

presented by Cooper et al. (2016)**, Hanson and Spetzler** (1994)**, and this study. (c) Schematic prediction of different responses during stress relaxation experiments. If steady state is reached before the backstress equals the applied stress, then subsequent relaxation will follow the plasticity flow law. If the backstress increases to equal the applied stress at the steady state, then subsequent load relaxation only results in forward strain as the backstress relaxes, following the steady-state power law.**

4.3 Consequences for transient creep in the upper mantle

590 Rheological models employed to analyze geodynamic scenarios vary widely in their form and behavior. In terms of models that capture transient behavior, by far the most common is the Burgers model, which contains two viscous elements, one describing the initial viscosity at the onset of loading and the other describing the steady-state viscosity. Burgers models (and related variations) have been calibrated for deformation of olivine dominated by diffusive mass transfer (e.g., Faul and Jackson, 2005; Sundberg and 595 Cooper, 2010) and by dislocation motion (Chopra, 1997). The former result in a linear viscoelastic model for which the viscosities do not depend on the level of stress applied, whereas the latter result in nonlinear viscoelastic models for which the viscosities are stress dependent. Linear viscoelastic models based on a Burgers model have been widely applied to a range of phenomena including glacial isostatic adjustment (e.g., Rumpker and Wolff, 1996; Yuen et al., 1986), postseismic creep (e.g., Hetland and Hager, 2005; 600 Pollitz et al., 2006), tidal dissipation (Bierson and Nimmo, 2016; e.g., Nimmo et al., 2012; Nimmo and Faul, 2013), and seismic attenuation (Carcione et al., 2014; Karato, 2012). Linear Burgers models have likely seen application to such a wide range of processes because of the relative mathematical ease of their implementation and the recognition that nonlinear viscoelasticity is generally restricted to large stress amplitudes, whereas most of these processes involve small stresses. However, nonlinear 605 viscoelastic models have seen increasing application to scenarios with larger stress changes, especially postseismic creep (Freed et al., 2012; Masuti et al., 2016). The viscosities in these nonlinear models are assumed to follow power laws, motivated by the power-law behavior of olivine during steady-state dislocation creep. However, the stress dependence is assumed to be the same for both the initial and the

steady-state viscosity. Therefore, in both linear and nonlinear Burgers models of upper mantle rocks, the ratio of the initial and steady-state viscosities is generally taken to be a constant.

Our results and analysis presented above demonstrate that the rheological behavior of olivine can be quite different than the behavior implemented in previous modelling efforts. As demonstrated by our data in Figure 6 and illustrated schematically in Figure 8a, during initial loading, we predict the strain rate of olivine to be close to linearly dependent on the stress at low stresses, with increasingly higher sensitivities to stress with increasing stress (Figure 6b also illustrates that the transition between linear and nonlinear behavior is not particularly dependent on temperature). Therefore, we predict the nonlinearity of the initial viscosity to be a function of the stress. This conclusion is particularly noteworthy because, for example, the apparent viscosity associated with geodynamic phenomena on short timescales could potentially follow linear viscoelastic behavior even when dislocation glide is the main strain producing process. Furthermore, if the nonlinearity of the initial viscosity is dependent on stress and temperature, then the ratio of the initial viscosity to the steady-state viscosity will also be a function of the stress.

5 Conclusions

Here we present a series of deformation experiments to investigate the microphysical mechanisms controlling transient creep in olivine. We conducted stress-reduction tests on olivine single crystals at elevated temperatures in a variety of crystal orientations. Our results reveal that stress-reductions are often accompanied by anelastic reverse strain. The magnitude of the reverse strain is dependent on the magnitude of the stress reduction. In certain crystal orientations, small stress reductions result in no reverse strain, indicating that a backstress is present in the crystals that is a fraction of the initially applied stress.

We recognise that deformation of olivine is fundamentally controlled by the glide velocity of dislocations, and therefore hypothesize that the low-temperature plasticity flow law calibrated at low temperatures can be extended to elevated temperatures. The buildup of backstresses associated with strain hardening in low-temperature plasticity is quantitatively consistent with the magnitudes of observed reverse strains. This hypothesis also predicts that the strain rates just after a stress reduction can be predicted with the low-temperature plasticity flow law, however, the existing flow law considerably overpredicts the strain rates observed here. Therefore, we recalibrate the activation energy of the low-temperature plasticity flow law to be consistent with initial strain rates in our experiments, initial strain rates in previously published high-temperature experiments, and yield stresses in low-temperature experiments.

We suggest that this recalibrated flow law can be used to predict the transient and steady-state creep strain rates by taking into account the evolution of the backstress and dislocation density. By combining the recalibrated flow law with previously published flow laws for the steady-state creep of olivine single crystals, we are able to correctly predict the magnitude of the observed backstress and its orientation dependence. We are also able to predict whether strain rates decrease (normal) or increase (inverse) during transient creep in our experiments and previously published experiments. This model also provides an explanation for the results of previous stress-relaxation experiments.

The results and analysis presented here indicate that the rheological behaviour of olivine during transient creep is fundamentally different from that incorporated into analyses of geodynamic processes. We suggest that the initial viscosity after a stress change, if controlled by dislocations, can range from linear to nonlinear, depending on the stress magnitude. Therefore, the ratio between the transient and steady-state viscosities is likely a function of the stress.

Acknowledgements

The authors benefited greatly from conversation with H. Jay Melosh on the rheological behavior of planetary bodies. His passing represents a great loss to our community. The authors would also like to acknowledge fruitful discussions with Reid Cooper, Ben Holtzman, and David Kohlstedt. LH and DW acknowledge support from the Natural Environment Research Council, grant NE/M000966/1, LH and CT acknowledge support from the Natural Environment Research Council, grant 1710DG008/JC4, and DW acknowledges support from the Netherlands Organisation for Scientific Research, User Support Programme Space Research, grant ALWGO.2018.038, and startup funds from Utrecht University. LH recognizes funds used to develop the uniaxial apparatus from the John Fell Fund at the University of Oxford. All data used in this study are available from the University of Minnesota Digital Conservancy (http://conservancy.umn.edu).

References

Abramson, E.H., Brown, J.M., Slutsky, L.J., Zaug, J., 1997. The elastic constants of San Carlos olivine to 17 GPa. J. Geophys. Res. [Solid Earth] 102, 12253–12263.

Ahlquist, C.N., Nix, W.D., 1971. The measurement of internal stresses during creep of Al and Al-Mg alloys. Acta Metall. 19, 373–385.

Argon, A.S., Takeuchi, S., 1981. Internal stresses in power-law creep. Acta Metallurgica. https://doi.org/10.1016/0001-6160(81)90113-9

Bai, Q., Kohlstedt, D.L., 1992a. High-temperature creep of olivine single crystals, 2. dislocation structures. Tectonophysics 206, 1–29.

Bai, Q., Kohlstedt, D.L., 1992b. High-temperature creep of olivine single crystals III. Mechanical results for unbuffered samples and creep mechanisms. Philos. Mag. A 66, 1149–1181.

Bai, Q., Mackwell, S.J., Kohlstedt, D.L., 1991. High-temperature creep of olivine single crystals 1. Mechanical results for buffered samples. J. Geophys. Res. [Solid Earth] 96, 2441–2463.

Bammann, D.J., 1989. A Micro-Mechanically Motivated Model of Finite Deformation Plasticity, in: Khan, A.S., Tokuda, M. (Eds.), Advances in Plasticity 1989. Pergamon, Oxford, pp. 283–286.

Benjamin Britton, T., Wilkinson, A.J., 2012. Stress fields and geometrically necessary dislocation density distributions near the head of a blocked slip band. Acta Mater. 60, 5773–5782.

Biberger, M., Gibeling, J.C., 1995. Analysis of creep transients in pure metals following stress changes. Acta Metallurgica et Materialia. https://doi.org/10.1016/0956-7151(95)00052-w

Bierson, C.J., Nimmo, F., 2016. A test for Io's magma ocean: Modeling tidal dissipation with a partially molten mantle. Journal of Geophysical Research: Planets. https://doi.org/10.1002/2016je005005

Blum, W., Finkel, A., 1982. New technique for evaluating long range internal back stresses. Acta Metall. 30, 1705–1715.

Blum, W., Weckert, E., 1987. On the interpretation of the "Internal stress" determined from dip tests during creep of Al-5at.%Mg. Materials Science and Engineering.

https://doi.org/10.1016/0025-5416(87)90449-6

Britton, T.B., Jiang, J., Guo, Y., Vilalta-Clemente, A., Wallis, D., Hansen, L.N., Winkelmann, A., Wilkinson, A.J., 2016. Tutorial: Crystal orientations and EBSD — Or which way is up? Mater. Charact. 117, 113–126.

Britton, T.B., Wilkinson, A.J., 2012. High resolution electron backscatter diffraction measurements of elastic strain variations in the presence of larger lattice rotations. Ultramicroscopy 114, 82–95.

Britton, T.B., Wilkinson, A.J., 2011. Measurement of residual elastic strain and lattice rotations with high resolution electron backscatter diffraction. Ultramicroscopy 111, 1395–1404.

Čadek, J., 1987. The back stress concept in power law creep of metals: A review. Int. J. Green Nanotech. Materials Sci. Eng. 94, 79–92.

Cao, R., Hansen, L.N., Thom, C.A., Wallis, D., 2020. An apparatus for measuring nonlinear viscoelasticity of minerals at high temperature. https://doi.org/10.31223/X59W2X

Carcione, J.M., Poletto, F., Farina, B., Craglietto, A., 2014. Simulation of seismic waves at the earth's crust (brittle-ductile transition) based on the Burgers model. Solid Earth 5, 1001.

Caswell, T.E., Cooper, R.F., Goldsby, D.L., 2015. The constant-hardness creep compliance of polycrystalline ice. Geophys. Res. Lett. 42, 6261–6268.

Chopra, P.N., 1997. High-temperature transient creep in olivine rocks. Tectonophysics. https://doi.org/10.1016/s0040-1951(97)00134-0

Cooper, R.F., Stone, D.S., Plookphol, T., 2016. Load relaxation of olivine single crystals. Journal of Geophysical Research: Solid Earth. https://doi.org/10.1002/2016jb013425

Durham, W.B., Goetze, C., 1977. Plastic flow of oriented single crystals of olivine: 1. Mechanical data. J. Geophys. Res. 82, 5737–5753.

Durham, W.B., Goetze, C., Blake, B., 1977. Plastic flow of oriented single crystals of olivine: 2. Observations and interpretations of the dislocation structures. Journal of Geophysical Research. https://doi.org/10.1029/jb082i036p05755

Evans, R.W., Roach, W.J.F., Wilshire, B., 1985. Creep of aluminium following stress reductions. Scr. Metall. 19, 999–1003.

Faul, U.H., Jackson, I., 2005. The seismological signature of temperature and grain size variations in the upper mantle. Earth Planet. Sci. Lett. 234, 119–134.

Field, E.H., Biasi, G.P., Bird, P., Dawson, T.E., Felzer, K.R., Jackson, D.D., Johnson, K.M., Jordan, T.H., Madden, C., Michael, A.J., Others, 2015. Long-term time-dependent probabilities for the third Uniform California Earthquake Rupture Forecast (UCERF3). Bull. Seismol. Soc. Am. 105, 511–543.

Field, E.H., Jordan, T.H., Page, M.T., Milner, K.R., Shaw, B.E., Dawson, T.E., Biasi, G.P., Parsons, T., Hardebeck, J.L., Michael, A.J., Weldon, R.J., Powers, P.M., Johnson, K.M., Zeng, Y., Felzer, K.R., van der Elst, N., Madden, C., Arrowsmith, R., Werner, M.J., Thatcher, W.R., 2017. A Synoptic View of the Third Uniform California Earthquake Rupture Forecast (UCERF3). Seismol. Res. Lett. 88, 1259–1267.

Freed, A.M., 2005. Earthquake Triggering by Static, Dynamic, and Postseismic Stress Transfer. Annu. Rev. Earth Planet. Sci. 33, 335–367.

Freed, A.M., Hirth, G., Behn, M.D., 2012. Using short-term postseismic displacements to infer the ambient deformation conditions of the upper mantle. J. Geophys. Res. 117. https://doi.org/10.1029/2011JB008562

Garmestani, H., Vaghar, M.R., Hart, E.W., 2001. A unified model for inelastic deformation of polycrystalline materials—application to transient behavior in cyclic loading and relaxation. Int. J. Plast. 17, 1367–1391.

Garofalo, F, 1963. An empirical relation defining the stress dependence of minimum creep rate in metals. Trans. AIME 227, 351–356.

Gibbs, G.B., 1966. Creep and stress relaxation studies with polycrystalline magnesium. The Philosophical

Magazine: A Journal of Theoretical Experimental and Applied Physics 13, 317–329.
Gibeling, J.C., Nix, W.D., 1981. Observations of anelastic backflow following stress reductions during creep of pure metals. Acta Metall. 29, 1769–1784.
Goetze, C., Kohlstedt, D.L., 1973. Laboratory study of dislocation climb and diffusion in olivine. J. Geophys. Res. 78, 5961–5971.
Gribb, T.T., Cooper, R.F., 1998. Low-frequency shear attenuation in polycrystalline olivine: Grain boundary diffusion and the physical significance of the Andrade model for viscoelastic rheology. Journal of Geophysical Research: Solid Earth. https://doi.org/10.1029/98jb02786
Gupta, I., Li, J.C.M., 1970. Stress relaxation, internal stress and work hardening in LiF and NaCl crystals. Int. J. Green Nanotech. Materials Sci. Eng. 6, 20–26.
Hansen, L.N., Kumamoto, K.M., Thom, C.A., Wallis, D., Durham, W.B., Goldsby, D.L., Breithaupt, T., Meyers, C.D., Kohlstedt, D.L., 2019. Low-temperature plasticity in olivine: Grain size, strain hardening, and the strength of the lithosphere. Journal of Geophysical Research: Solid Earth. https://doi.org/10.1029/2018jb016736
Hanson, D.R., Spetzler, H.A., 1994. Transient creep in natural and synthetic, iron-bearing olivine single crystals: Mechanical results and dislocation microstructures. Tectonophysics. https://doi.org/10.1016/0040-1951(94)90191-0
Hart, E.W., 1976. Constitutive Relations for the Nonelastic Deformation of Metals. J. Eng. Mater. Technol. 98, 193–202.
Hart, E.W., 1970. A phenomenological theory for plastic deformation of polycrystalline metals. Acta Metall. 18, 599–610.
Hetland, E.A., Hager, B.H., 2005. Postseismic and interseismic displacements near a strike-slip fault: A two-dimensional theory for general linear viscoelastic rheologies. J. Geophys. Res. [Solid Earth] 110.
Hirth, G., Kohlstedt, D., 2003. Rheology of the upper mantle and the mantle wedge: A view from the experimentalists, in: Eiler, J. (Ed.), Geophysical Monograph Series. American Geophysical Union, Washington, D. C., pp. 83–105.
Hunter, J., Watts, A.B., 2016. Gravity anomalies, flexure and mantle rheology seaward of circum-Pacific trenches. Geophys. J. Int. 207, 288–316.
Jackson, I., Faul, U.H., Skelton, R., 2014. Elastically accommodated grain-boundary sliding: New insights from experiment and modeling. Phys. Earth Planet. Inter. 228, 203–210.
Jackson, I., Fitz Gerald, J.D., Faul, U.H., Tan, B.H., 2002. Grain-size-sensitive seismic wave attenuation in polycrystalline olivine. Journal of Geophysical Research: Solid Earth. https://doi.org/10.1029/2001jb001225
Karato, S.-I., 2012. On the origin of the asthenosphere. Earth Planet. Sci. Lett. 321, 95–103.
Karato, S.-I., Paterson, M.S., FitzGerald, J.D., 1986. Rheology of synthetic olivine aggregates: Influence of grain size and water. J. Geophys. Res. 91, 8151–8176.
Karato, S.-I., Rubie, D.C., Yan, H., 1993. Dislocation recovery in olivine under deep upper mantle conditions: Implications for creep and diffusion. J. Geophys. Res. 98, 9761–9768.
Karato, S., Spetzler, H.A., 1990. Defect microdynamics in minerals and solid-state mechanisms of seismic wave attenuation and velocity dispersion in the mantle. Reviews of Geophysics. https://doi.org/10.1029/rg028i004p00399
Kassner, M.E., 2015. Fundamentals of Creep in Metals and Alloys. Butterworth-Heinemann.
Kocks, U.F., Argon, A.S., Ashby, M.F., 1975. Thermodynamics and Kinetics of Slip. Prog. Mater Sci. 19.
Korhonen, M.A., Hannula, S.-P., Li, C.-Y., 1987. State variable theories based on Hart's formulation, in: Unified Constitutive Equations for Creep and Plasticity. Springer, pp. 89–137.
Masuti, S., Barbot, S.D., Karato, S.-I., Feng, L., Banerjee, P., 2016. Upper-mantle water stratification inferred from observations of the 2012 Indian Ocean earthquake. Nature 538, 373–377.

Masuti, S., Karato, S.-I., Girard, J., Barbot, S.D., 2019. Anisotropic high-temperature creep in hydrous olivine single crystals and its geodynamic implications. Phys. Earth Planet. Inter. 290, 1–9.

Mecking, H., Kocks, U.F., 1981. Kinetics of flow and strain-hardening. Acta Metallurgica. https://doi.org/10.1016/0001-6160(81)90112-7

Menezes, R.A., Nix, W.D., 1971. Average internal stresses in LiF single crystals during high temperature creep. Acta Metall. 19, 645–649.

Meyssonnier, J., Goubert, A., 1994. Transient creep of polycrystalline ice under uniaxial compression: an assessment of internal state variable models. Annals of Glaciology. https://doi.org/10.1017/s0260305500010983

Milička, K., Trojanová, Z., Lukáč, P., 2007. Internal stresses during creep of magnesium alloys at 523 K. Materials Science and Engineering: A 462, 215–219.

Mughrabi, H., 1980. Strength of metals and alloys, in: Proc. Intern. Conf. Metals and Alloys, Ed. by P. Haasen, V. Gerold and G. Kostorz, Pergamon, Oxford. p. 1615.

Müller, W., Biberger, M., Blum, W., 1992. Subgrain-boundary migration during creep of lif III. Stress reduction experiments. Philosophical Magazine A. https://doi.org/10.1080/01418619208201586

Nimmo, F., Faul, U.H., 2013. Dissipation at tidal and seismic frequencies in a melt-free, anhydrous Mars. Journal of Geophysical Research: Planets 118, 2558–2569.

Nimmo, F., Faul, U.H., Garnero, E.J., 2012. Dissipation at tidal and seismic frequencies in a melt-free Moon. Journal of Geophysical Research: Planets 117.

Nix, W.D., Ilschner, B., 1979. Mechanisms Controlling Creep of Single Phase Metals and Alloys, in: Haasen, P., Gerold, V., Kostorz, G. (Eds.), Strength of Metals and Alloys. Pergamon, pp. 1503–1530.

Poirier, J.P., 1977. Microscopic creep models and the interpretation of stress-drop tests during creep. Acta Metallurgica. https://doi.org/10.1016/0001-6160(77)90178-x

Pollitz, F.F., 2005. Transient rheology of the upper mantle beneath central Alaska inferred from the crustal velocity field following the 2002 Denali earthquake. J. Geophys. Res. 110. https://doi.org/10.1029/2005jb003672

Pollitz, F.F., Bürgmann, R., Banerjee, P., 2006. Post-seismic relaxation following the great 2004 Sumatra-Andaman earthquake on a compressible self-gravitating Earth. Geophys. J. Int. 167, 397–420.

Post, R.L., Jr., 1977. High-temperature creep of Mt. Burnet dunite. Tectonophysics 42, 75–110.

Qiu, Q., Moore, J.D.P., Barbot, S., Feng, L., Hill, E.M., 2018. Transient rheology of the Sumatran mantle wedge revealed by a decade of great earthquakes. Nat. Commun. 9, 995.

Rumpker, G., Wolff, D., 1996. Viscoelastic relaxation of a Burgers half-space: implications for the interpretation of the Fennoscandian uplift. Geophysical Journal International. https://doi.org/10.1111/j.1365-246x.1996.tb07036.x

Smith, B.K., Carpenter, F.O., 1987. Transient creep in orthosilicates. Physics of the Earth and Planetary Interiors. https://doi.org/10.1016/0031-9201(87)90033-1

Stone, D.S., 1991. Scaling laws in dislocation creep. Acta Metall. Mater. 39, 599–608.

Stone, D.S., Plookphol, T., Cooper, R.F., 2004. Similarity and scaling in creep and load relaxation of single-crystal halite (NaCl). J. Geophys. Res. [Solid Earth] 109.

Sundberg, M., Cooper, R.F., 2010. A composite viscoelastic model for incorporating grain boundary sliding and transient diffusion creep; correlating creep and attenuation responses for materials with a fine grain size. Philos. Mag. 90, 2817–2840.

Takeuchi, S., Argon, A.S., 1976. Steady-state creep of single-phase crystalline matter at high temperature. J. Mater. Sci. 11, 1542–1566.

Taylor, G.I., 1934. The mechanism of plastic deformation of crystals. Part I.—Theoretical. Proceedings of the Royal Society of London. Series A, Containing Papers of a Mathematical and Physical Character 145, 362–387.

Thieme, M., Demouchy, S., Mainprice, D., Barou, F., Cordier, P., 2018. Stress evolution and associated microstructure during transient creep of olivine at 1000–1200 °C. Physics of the Earth and Planetary Interiors. https://doi.org/10.1016/j.pepi.2018.03.002

Toriumi, M., Karato, S.-I., 1978. Experimental studies on the recovery process of deformed olivines and the mechanical state of the upper mantle. Tectonophysics 49, 79–95.

Wallis, D., Hansen, L.N., Ben Britton, T., Wilkinson, A.J., 2017. Dislocation Interactions in Olivine Revealed by HR-EBSD. J. Geophys. Res. [Solid Earth] 122, 7659–7678.

Wallis, D., Hansen, L.N., Ben Britton, T., Wilkinson, A.J., 2016. Geometrically necessary dislocation densities in olivine obtained using high-angular resolution electron backscatter diffraction. Ultramicroscopy 168, 34–45.

Wallis, D., Hansen, L.N., Britton, T.B., Wilkinson, A.J., 2019. High-Angular Resolution Electron Backscatter Diffraction as a New Tool for Mapping Lattice Distortion in Geological Minerals. Journal of Geophysical Research: Solid Earth. https://doi.org/10.1029/2019jb017867

Wallis, D., Hansen, L.N., Kumamoto, K.M., Thom, C.A., Plümper, O., Ohl, M., Durham, W.B., Goldsby, D.L., Armstrong, D.E.J., Meyers, C.D., Goddard, R.M., Warren, J.M., Breithaupt, T., Drury, M.R., Wilkinson, A.J., 2020a. Dislocation interactions during low-temperature plasticity of olivine and their impact on the evolution of lithospheric strength. Earth Planet. Sci. Lett. 543, 116349.

Wallis, D., Hansen, L.N., Wilkinson, A.J., Lebensohn, R.A., 2020b. Dislocation interactions in olivine control postseismic creep of the upper mantle. arXiv [cond-mat.mtrl-sci].

Wang, L., Blaha, S., Pintér, Z., Farla, R., Kawazoe, T., Miyajima, N., Michibayashi, K., Katsura, T., 2016. Temperature dependence of [100](010) and [001](010) dislocation mobility in natural olivine. Earth Planet. Sci. Lett. 441, 81–90.

Wang, Z., Karato, S.-I., Fujino, K., 1996. High temperature creep of single crystal gadolinium gallium garnet. Physics and Chemistry of Minerals. https://doi.org/10.1007/bf00202301

Wang, Z., Karato, S.-I., Fujino, K., 1993. High temperature creep of single crystal strontium titanate (SrTiO3): a contribution to creep systematics in perovskites. Phys. Earth Planet. Inter. 79, 299–312.

Wilkinson, A.J., Meaden, G., Dingley, D.J., 2006. High-resolution elastic strain measurement from electron backscatter diffraction patterns: new levels of sensitivity. Ultramicroscopy 106, 307–313.

Yuen, D.A., Sabadini, R.C.A., Gasperini, P., Boschi, E., 1986. On transient rheology and glacial isostasy. J. Geophys. Res., Geophys. Monogr 91, 11420.

Zhong, S., Watts, A.B., 2013. Lithospheric deformation induced by loading of the Hawaiian Islands and its implications for mantle rheology. J. Geophys. Res. [Solid Earth] 118, 2013JB010408.